nature materials

Article

https://doi.org/10.1038/s41563-025-02461-x

Nonlinear phase-matched van der Waals crystals integrated on optical fibres

Received: 3 January 2025

Accepted: 3 December 2025

Published online: 13 January 2026

Check for updates

Kaifeng Lin[1,2,11], Guangjie Yao[1,2,11], Jiahui Shao[1,2,11], Yilong You[1,11], Jiajie Qi[1], Daopeng Yuan[3], Yijun Wang[1], Muhong Wu[4], Lingjun Kong[5], Xiangdong Zhang[5], Enge Wang[6,7], Zhipei Sun[8] ✉, Hao Hong[1,9] ✉ & Kaihui Liu[1,6,10] ✉

High optical nonlinearity can enable classical and quantum functionalities in all-fibre laser systems. However, despite long-standing efforts to exploit second-order optical nonlinearity in conventional all-fibre systems, nonlinear optical conversion efficiencies remain modest. Here we demonstrate all-fibre integration of twist-phase-matched rhombohedral boron nitride (rBN) flakes on the end facet of optical fibres for second-harmonic generation (SHG) and spontaneous parametric downconversion (SPDC). We provide local and global optimization of the interflake twist angles for phase-matching design, achieving an SHG conversion efficiency of ~4.1% and an SPDC coincidence rate of ~90 in van der Waals crystals integrated on optical fibre devices. Finally, we design an all-fibre frequency-doubling ultrafast laser by integrating a multifunctional nonlinear crystal of a graphene/rBN heterostructure to simultaneously generate mode-locked pulses and intracavity SHG emission. This work establishes a route for developing high-efficiency, second-order nonlinear functionalities, such as optical parametric oscillators, optical modulators and entangled photon sources, in all-fibre lasers.

Complete functionalities in all-optical fibre systems analogous to those in free-space lasers are highly desirable because of the superior output mode quality, excellent stability and portability. So far, functional components for laser generation, amplification, mode locking and four-wave mixing have been successfully developed and widely implemented in fibre lasers[1–8]. However, the second-order nonlinearity—the fundamental and lowest order nonlinear effect—for second-harmonic generation (SHG), spontaneous parametric downconversion (SPDC) and electro-optic modulation is lacking, owing to the centrosymmetric structure of silica material. Two main approaches to add second-order nonlinearity to optical fibres have been proposed: poling and decorating the fibres. Poling silica fibres requires complex processing to break the geometric symmetry at the silica/air interface for SHG and SPDC, but can only offer limited nonlinearity ($\chi^{(2)} \approx 0.02$ pm V^{-1}) and a very narrow working bandwidth (of a few nanometres)[9–12]. Decorating optical fibres with nonlinear materials can impart high optical nonlinearities and support broad bandwidth operation for both continuous-wave and pulsed fibre lasers[13–21]. However, the overall energy conversion efficiency

[1]State Key Lab for Mesoscopic Physics and Frontiers Science Center for Nano-optoelectronics, School of Physics, Peking University, Beijing, China. [2]Academy for Advanced Interdisciplinary Studies, Peking University, Beijing, China. [3]Taishan College, Shandong University, Jinan, China. [4]Institute of Atomic Manufacturing, International Institute for Interdisciplinary and Frontiers, Beihang University, Beijing, China. [5]Key Laboratory of Advanced Optoelectronic Quantum Architecture and Measurements of Ministry of Education, School of Physics, Beijing Institute of Technology, Beijing, China. [6]International Centre for Quantum Materials, Collaborative Innovation Centre of Quantum Matter, Peking University, Beijing, China. [7]Tsientang Institute for Advanced Study, Hangzhou, China. [8]QTF Centre of Excellence, Department of Electronics and Nanoengineering, Aalto University, Espoo, Finland. [9]Interdisciplinary Institute of Light-Element Quantum Materials and Research Centre for Light-Element Advanced Materials, Peking University, Beijing, China. [10]Songshan Lake Materials Lab, Dongguan, China. [11]These authors contributed equally: Kaifeng Lin, Guangjie Yao, Jiahui Shao, Yilong You. ✉e-mail: zhipei.sun@aalto.fi; haohong@pku.edu.cn; khliu@pku.edu.cn

remains quite low (typically <0.1%) owing to mode leakage and/or weak light–matter interactions in the specialized fibres used for integration, such as photonic crystal fibres, exposed-core fibres or hollow-core fibres.

In principle, the end facet of an optical fibre is considered an ideal platform for the integration of nonlinear optical crystals, as it provides tight focusing for strong interactions, a well-defined optical mode for excitation and mature fibre fusion technology[22–25]. However, all traditional nonlinear optical crystals, such as β-barium borate and lithium niobate, are not compatible with silica-based device fabrication, as the typical thickness of these crystals is more than a few millimetres, which results in large optical coupling losses due to mode divergence. Moreover, these conventional crystals with strong in-plane anisotropy require accurate polarization control for excitation, which further complicates the all-fibre system (Supplementary Fig. 1).

Fortunately, emerging van der Waals (vdW) crystals provide new opportunities to decorate fibres, mainly owing to their excellent integration ability and ultrahigh optical nonlinearity[26–34]. The atomically flat surfaces preserve high-quality optical modes within fibres, while their huge in-plane nonlinear coefficients, which are 1–3 orders of magnitude larger than those of traditional materials[28], enable a ~1% SHG efficiency within a thickness of only a few micrometres[33].

For an efficient parametric process, a phase-matching design is a prerequisite[35–41]. This design involves establishing a proper phase relationship between the fundamental wave (FW) and SHG wave to enable continuous SHG enhancement over the transmission. In the architecture of fibre–vdW crystal–fibre SHG components, birefringent phase matching is initially excluded because of the low in-plane birefringence of vdW crystals. Quasi-phase matching requires electric dipole inversion at a specific crystal thickness (that is, the coherence length), which is extremely difficult to realize in sample preparation with current growth methods. The recently developed twist-phase matching is not directly applicable either[41], as achieving the required circularly polarized light in a usual fibre system is challenging. Therefore, a new phase-matching strategy for the fibre end facet integration architecture urgently needs to be developed for the design of high-efficiency all-fibre optical nonlinear components.

Here we developed a phase-matching method in an optical fibre system by vertically stacking several twisted rhombohedral boron nitride (rBN) flakes under linearly polarized FW excitation. We found that the series of stacking twist angles substantially differed when the flakes were added sequentially for local optimization or when all the flakes were considered as an entity for global optimization to maximize the SHG output. Guided by this model, we fabricated all-fibre SHG and SPDC components by integrating twisted rBN between two fibre end facets, and realized an SHG conversion efficiency of ~4.1% (values <0.1% have been reported for vdW crystals on optical fibres[16–20]), achieving a compact all-fibre-based quantum light source and an all-fibre frequency-doubling ultrafast laser.

Results and discussion

Phase-matching design on the fibre end facet

The all-fibre SHG component is designed by sandwiching rBN single-crystal flakes between the end facets of two single-mode optical fibres (Fig. 1a). Owing to the large nonlinear coefficient ($\chi^{(2)} \approx 30$ pm V^{-1}) and high laser-induced damage threshold (~100 GW cm^{-2}) of rBN, high-efficiency SHG exceeding 6% can theoretically be achieved within a thickness of ~8.5 μm (Supplementary Note 1). The small thickness of rBN, together with its close refractive index to that of the optical fibres ($n_{rBN} \approx 2.08$, $n_{fibre} \approx 1.45$, at $\lambda_{FW} = 1{,}064$ nm), provides a low divergence of the transmitting light (shown as dashed lines in Fig. 1c) and slight multiple reflection effects between the two interfaces of the fibre/rBN/fibre device (shown as fluctuations in the curves in Fig. 1b,d and Supplementary Fig. 2). The estimated total insertion loss of the device is ~7% (0.3 dB) after the insertion of a 20-μm-thick rBN crystal (Fig. 1b).

Figure 1c presents the intensity distributions of the FW and SHG in a fibre/20-μm-thick rBN/fibre assembly from our simulation. The FW exhibits a nearly uniform distribution within the rBN crystal (Fig. 1c, left). By contrast, the SHG intensity displays a sinusoidal-like oscillation as the transmission length increases, indicating the presence of phase mismatch during nonlinear parametric processes (Fig. 1c, middle). The coherence length (distance between the initial point and the first maximum value point) is determined to be $L_c = 4.25$ μm. To achieve constructive SHG enhancement, quasi-phase matching can be employed by rotating the rBN lattice between adjacent flakes by 60° (equivalent to 180° in rBN with C_3 symmetry) for each coherence length (Fig. 1c, right). As anticipated, a continuous increase in the SHG intensity can be observed (Fig. 1d).

However, experimentally, directly growing or exfoliating rBN with an accurate thickness of L_c is quite challenging. For more general cases, stacking rBN flakes with arbitrary thickness (t) and adjustable twist angle (θ) allows us to exceed this limit. First, we consider the basic situation of the stacking of two flakes (Fig. 2a). We decompose the linearly polarized FW electric field to be a superposition of the left and right circularly polarized electric fields ($\mathbf{E}^+_\omega$ and $\mathbf{E}^-_\omega$). From the perspective of circular polarization, the output SHG signal is predicted to be

$$\mathbf{E}^-_{2\omega} = \frac{\sqrt{2}\omega}{cn(2\omega)}\chi^{(2)}\left(\mathbf{E}^+_\omega\right)^2\left(\frac{1-e^{-i\Delta kt}}{\Delta k} + \frac{e^{-i\Delta kt}-e^{-i2\Delta kt}}{\Delta k}e^{i3\theta}\right) \quad (1)$$

$$\mathbf{E}^+_{2\omega} = \frac{\sqrt{2}\omega}{cn(2\omega)}\chi^{(2)}\left(\mathbf{E}^-_\omega\right)^2\left(\frac{1-e^{-i\Delta kt}}{\Delta k} + \frac{e^{-i\Delta kt}-e^{-i2\Delta kt}}{\Delta k}e^{-i3\theta}\right) \quad (2)$$

where $\mathbf{E}^-_{2\omega}$ ($\mathbf{E}^+_{2\omega}$) and $\mathbf{E}^-_\omega$ ($\mathbf{E}^+_\omega$) are the left (right) circularly polarized electric fields of the SHG and FW, respectively. c is the speed of light in vacuum, $n_{2\omega}$ is the refractive index for the SHG light and $\Delta k = k_{2\omega} - 2k_\omega$ is the wavevector mismatch of the SHG and FW. This equation indicates that the twist angle θ results in a 3θ (-3θ) phase shift in the $\mathbf{E}^-_{2\omega}$ ($\mathbf{E}^+_{2\omega}$) of the second flake[41].

A physical representation of the effect of θ on the SHG intensity in a stacked two-flake system is illustrated in the complex amplitude diagram shown in Fig. 2b. $\mathbf{E}^-_{2\omega}$ and $\mathbf{E}^+_{2\omega}$ can be directly derived from the geometry. The overall SHG intensity is the combination of both left and right circularly polarized components, which is determined as $\mathbf{I}_{2\omega} \propto |\mathbf{E}^-_{2\omega}|^2 + |\mathbf{E}^+_{2\omega}|^2$. The θ-dependent and t-dependent SHG intensity under linearly polarized FW excitation of two flakes is shown in Fig. 2c. The SHG intensity reaches its maximum when θ equals 0° or 60° for t less than or greater than $0.5L_c$, respectively.

When stacking more than two flakes, in which the qth added flake with thickness t is rotated by an angle θ_q relative to the first flake, two distinct strategies emerge: (1) local optimization stacking, in which each flake is sequentially added, and the present SHG intensity is maximized by tuning the angle θ_q of the newly added flake (Fig. 2d); and (2) global optimization stacking, in which all flakes are considered as an entity and the overall SHG intensity is maximized by tuning all the stacking angles (Fig. 2g).

In the local optimization stacking design, the SHG output intensities and the stacking twist-angle strategy can be directly predicted from the geometry, the same as in the situation for two flakes demonstrated in Fig. 2b (see Supplementary Note 2a). An angle of 0° or 60° can be shown to be always the optimal angle to achieve the maximum SHG value (Supplementary Note 2b). Thus, $\mathbf{E}^-_{2\omega}$ and $\mathbf{E}^+_{2\omega}$ become equivalent. Experimentally, we built a homemade in situ transfer system to simultaneously rotate the angle θ_q and monitor the SHG intensity (see Methods and Supplementary Fig. 3 for details). The rBN flakes were stacked to achieve the maximum SHG intensity as the twist angles θ_q were rotated (the SHG signal generated by the bare fibre was negligible; Supplementary Fig. 4). For two flakes with a uniform thickness of $0.4L_c$ (determined by atomic force microscope mapping in Supplementary Fig. 5), the SHG intensity reaches a maximum at 0° (Fig. 2e). In the case of a total of five flakes, we found a twist-angle

https://doi.org/10.1038/s41563-025-02461-x

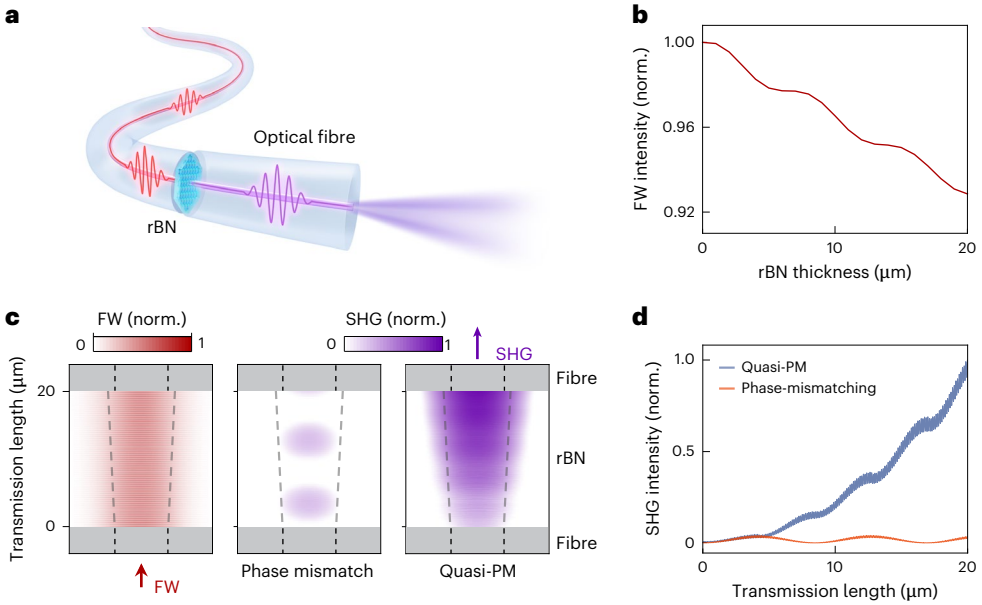


Fig. 1 | Van der Waals crystal integrated on optical fibre. a, Schematic representation of rBN embedded between the optical fibre end facet. Pulsed light is directly frequency doubled by a rBN nonlinear crystal during propagation in the optical fibre. **b**, Dependence of FW transmittance on the thickness of rBN between optical fibres from simulation. **c**, Simulated optical intensity distribution of FW (left panel), SHG under phase mismatch (PM) (middle panel) and SHG with quasi-phase matching (right panel). **d**, Simulated SHG intensity as a function of transmission length. All the above simulations were performed with an incident wavelength of 1,064 nm. norm., normalized.

sequence of (0°, 0°, 60°, 60°, 0°) (Fig. 2f). For comparison of the efficiency between different methods, we plot the quasi-phase-matching curve, which is described by the following equation

$$I_{\mathrm{SHG}} \propto \left(\int_0^T d_{\mathrm{eff}}(t) \times \mathrm{e}^{i\Delta k t} \mathrm{d}t \right)^2, \tag{3}$$

where T is the total thickness and $d_{\mathrm{eff}}(t)$ represents a periodic modulation taking values of either +1 or −1. Whenever dt advances by L_c, the sign of $d_{\mathrm{eff}}(t)$ is reversed. Notably, the stacked system has a slightly lower efficiency than that in the quasi-phase-matching condition.

In the global optimization stacking design, the rotation angles of each flake θ_q are optimized to achieve the overall maximum SHG output rather than the maximum in every intermediate step (Fig. 2g). The total intensity of N flakes is expressed as

$$\mathbf{E}^{-}_{2\omega,\mathrm{N}} = \frac{i\sqrt{2}\omega}{cn(2\omega)} \chi^{(2)} \left(\mathbf{E}^{+}_{\omega}\right)^2 \sum_{q=1}^{q=N} \frac{i}{\Delta k} \mathrm{e}^{i3\theta_q} \left(\mathrm{e}^{-i\Delta k t_q} - 1\right) \mathrm{e}^{-i\Delta k \sum_{p=1}^{p=q-1} t_p} \tag{4}$$

$$\mathbf{E}^{+}_{2\omega,\mathrm{N}} = \frac{i\sqrt{2}\omega}{cn(2\omega)} \chi^{(2)} \left(\mathbf{E}^{-}_{\omega}\right)^2 \sum_{q=1}^{q=N} \frac{i}{\Delta k} \mathrm{e}^{-i3\theta_q} \left(\mathrm{e}^{-i\Delta k t_q} - 1\right) \mathrm{e}^{-i\Delta k \sum_{p=1}^{p=q-1} t_p} \tag{5}$$

In this case, 0° or 60° is no longer the best setting, and $\mathbf{E}^{-}_{2\omega}$ and $\mathbf{E}^{+}_{2\omega}$ cannot be easily predicted from the geometry. As equations (4) and (5) are quite complex for an analytical solution, we obtain the globally optimized stacking sequence through a theoretical traversal (Supplementary Note 3). For $N = 3$ and $t = 0.4L_c$, we obtain an optimal sequence of (0°, 26°, 53°), as shown in Fig. 2h, in contrast to the optimal sequence of (0°, 0°, 60°) obtained in the local optimization stacking. For $N = 5$ and $t = 0.4L_c$, (0°, 24°, 48°, 72°, 96°) is the optimal sequence for the maximum SHG intensity. Experimentally, we transferred twisted rBN flakes accordingly and found a higher conversion efficiency than that in quasi-phase matching (Fig. 2i and Supplementary Fig. 6). We note that the SHG intensity of the stacked flakes is quite robust against the deviations in thickness and twist angle (Supplementary Fig. 7).

SPDC and SHG performance in twisted rBN fibre

Utilizing the phase-matched design for enhanced optical nonlinearity, the reverse process of SHG (that is, SPDC) can also be efficiently realized in our vdW crystals integrated optical fibre devices (Fig. 3a; see Supplementary Fig. 8 and Methods for details). Photon pairs at 810 nm were generated and detected under 405-nm light excitation (Fig. 3b). A clear temporal coincidence peak was observed (Fig. 3c), with the coincidence rate increasing linearly with pump power (Fig. 3d). The second-order correlation function at zero time delay, $g^2(0)$, decreases inversely with increasing pump power up to 10 mW (Fig. 3e), indicating robust photon pair generation across a wide excitation power range. We note that vdW crystals have been demonstrated to be ideal platforms for fabricating ultrathin quantum light sources[32,42–44]. Here we applied twist phase matching for SPDC and highlighted the notable potential for seamless integration of vdW crystals into fibre-based quantum communication networks (see Supplementary Table 1 for comparison with the four-wave mixing method).

Compared with fibre systems relying on free-space alignment optics, all-fibre systems have extremely high stability in different environments. Currently, available micro/nanostructure optical fibres and D-shaped fibres are highly compatible with the integration of nonlinear materials. However, these specially structured fibres are relatively fragile, and their optical modes are susceptible to environmental fluctuations. Our end facet integration architecture on single-mode fibres is clearly, in principle, quite robust. The encapsulation between the fibres provides good protection of the nonlinear crystal from oxidation and deliquescence. Figure 4a shows an optical image of the fibre/rBN assembly and its SHG (532 nm) output spot.

https://doi.org/10.1038/s41563-025-02461-x

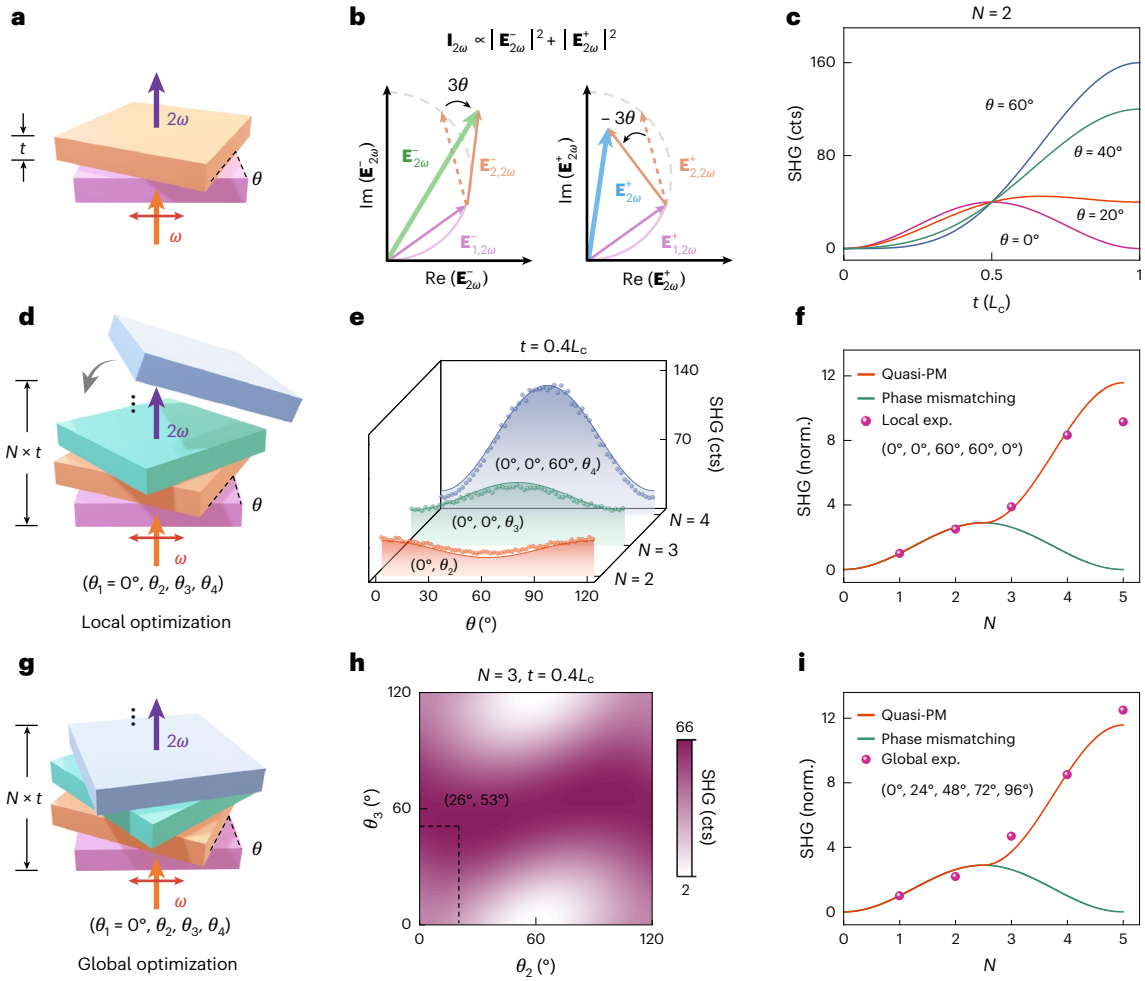


Fig. 2 | Nonlinear phase-matching design for the twisted van der Waals crystal integrated on optical fibre. a, Schematic of twisted two flakes of rBN for SHG under linearly polarized excitation. The flakes have a relative twist angle of θ and an identical thickness of t. **b**, Illustration of the physical picture of the twisted rBN for SHG. Linearly polarized excitation can be divided into two circularly polarized components ($\mathbf{E}^-$ and $\mathbf{E}^+$). The magenta vector represents the response of the first flake, and the orange vector for the second flake. The dotted line is the original vector without twist ($\theta = 0°$), which is rotated with an angle of 3θ (-3θ) after interflake twist for left (right) circularly polarized components. The horizontal and vertical axes correspond to the real part (Re) and imaginary part (Im) of the complex SHG field amplitude, respectively. **c**, Calculated SHG intensity of twist-rBN shown in **a** with different θ and t. **d**, Schematic of local optimization. N pieces of rBN flakes are added sequentially to maximize SHG intensity by tuning the new added angle. **e**, Theoretical (solid curves) and experimental (dots) results under local optimization for phase matching with $t = 0.4L_c$. Highest efficiency is achieved at either 0° or 60°. **f**, Experimental data (dots) for stacking using local optimization. **g**, Schematic of global optimization. N pieces of rBN flakes are considered as an entity to maximize SHG intensity by tuning all the stacking angles. **h**, Simulation of global optimization for phase matching with $N = 3$ and $t = 0.4L_c$. Maximum intensity appears at angel sequence of (26°, 53°). **i**, Experimental data (dots) for stacking using global optimization. Twist-rBN with an angle sequence of (0°, 24°, 48°, 72°, 96°) provides a higher SHG intensity than that of quasi-phase matching. All the above experiments were conducted with an incident wavelength of 1,064 nm. cts, counts.

A perfect Gaussian profile is achieved for SHG by integrating four flakes of twisted rBN with a total thickness of ~8.5 μm.

Then, we used UV-curable adhesive to encapsulate the twisted rBN flakes between the two fibre end facets to form an all-fibre device (see Methods and Supplementary Fig. 9 for details). The excitation peak intensity-dependent conversion efficiency of the fabricated fibre/twisted rBN/fibre SHG component is shown in Fig. 4b. Before the laser-induced damage threshold at 224 mW (~80 GW cm^{-2}), the conversion efficiency reaches a value of ~4.1% for pulsed SHG under global optimization phase-matching design, corresponding to 9.2 mW (~3.3 GW cm^{-2}) (Supplementary Fig. 10 and see Supplementary Table 2 for comparison). This high-quality SHG output demonstrates remarkable stability over time and with respect to acceleration, temperature and humidity. The SHG fluctuations are confined within ±0.1% for 5 h monitoring, and the reduction remains below 3% with more than 3 weeks of continuous operation (Fig. 4c). The component operates reliably at accelerations of up to 50 m s^{-2} (Fig. 4d), temperatures ranging from −20 °C to 90 °C (Fig. 4e) and humidities of up to 100% (Fig. 4f). In addition, owing to the flat chromatic dispersion of rBN and the ultrathin total thickness, the calculated working bandwidth of our phase-matched fibre/rBN/fibre SHG component exceeds 200 nm (Supplementary Fig. 11).

All-fibre frequency-doubling pulsed laser

The all-fibre SHG component with large optical nonlinearity, a high-quality optical mode, ultimate stability and a broad phase-matching bandwidth is suitable for an all-fibre intracavity frequency conversion laser. We thus designed a fibre ring cavity to fabricate an all-fibre frequency-doubling pulsed laser (Fig. 5a). In addition to a pump laser diode (980 nm continuous-wave laser), an erbium-doped fibre (serving as the gain media) and an optical coupler (for laser output), a heterostructure composed of 10 layers of graphene and 4 flakes of twisted rBN was integrated into the fibre ring cavity for mode locking and intracavity frequency conversion, respectively

https://doi.org/10.1038/s41563-025-02461-x

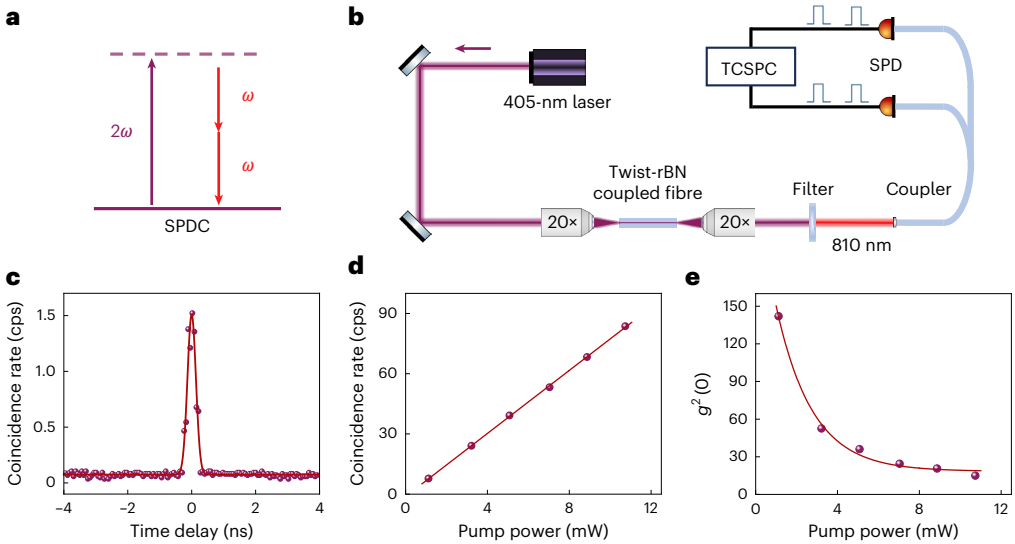


Fig. 3 | Integrated twist-rBN on the optical fibre for photon pair generation through SPDC. a, Half-frequency photon pair generation of the SPDC process. **b**, Illustration of the optical setup for SPDC measurement. The band-pass filter is centred at 810 nm with a 3-nm full-width at half-maximum; fibre coupler is 50:50; SPD, single-photon detector; TCSPC, time-correlated single-photon counting. **c**, Normalized coincidence measurement. The coincidence count rate notably surpasses ~1.5 Hz with 1.12-mW excitation. cps, counts per second. **d**, Coincidence rate as a function of pump power, which exhibits a linear dependence. **e**, Correlation measurement ($g^2(0)$) as a function of pump power, which exhibits a reverse dependence.

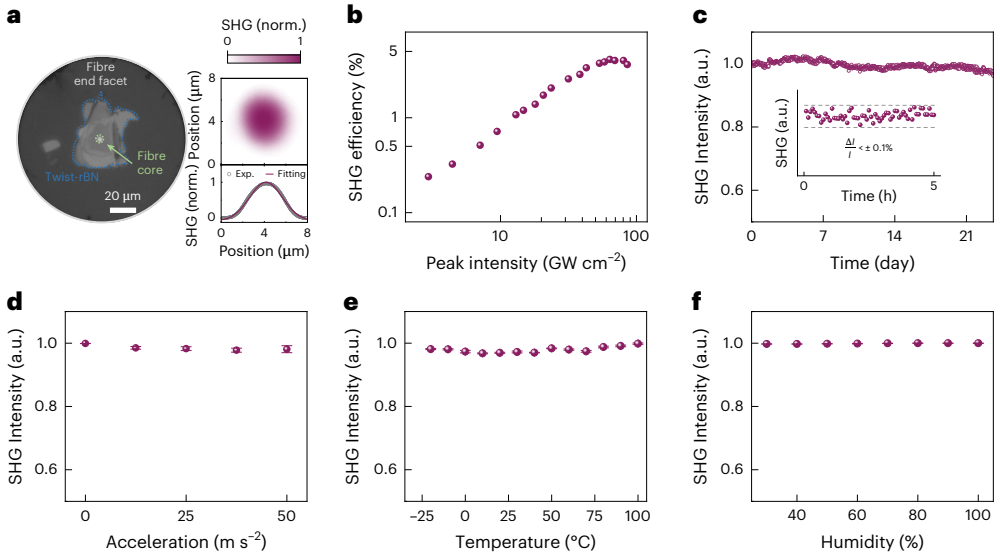


Fig. 4 | SHG performance of twist-rBN integrated on optical fibre. a, SHG output of twist-rBN integrated optical fibre. Left: optical image of twist-rBN on optical fibre. Right: lateral intensity distribution of SHG output with a perfect Gaussian-like fundamental mode. **b**, Dependence of SHG conversion efficiency on FW peak intensity. The maximum SHG conversion efficiency of the twist-rBN fibre is determined to be ~4.1% under excitation near the damage threshold of rBN at ~80 GW cm^{-2}. **c**, Long-term SHG output stability. A total SHG intensity decrease of less than 3% is observed during the whole test over 3 weeks. The inset shows the fluctuation is less than ±0.1% for 5 h monitoring. **d**–**f**, High-stability SHG output under perturbation of acceleration (**d**), temperature (**e**) and humidity (**f**). The error bars are obtained by monitoring the intensity fluctuation for 1 h under each condition, with the fluctuation quantified by the standard deviation across 360 data points. The maximum fluctuation is 1.1%, 0.4% and 0.1%, respectively. All the above experiments were conducted with an incident wavelength of 1,064 nm. Except for the experiment shown in **a**, all other measurements use the encapsulated fibre. Exp., experiment.

(Supplementary Fig. 12). The saturable absorption behaviour of the fibre-based heterostructure is shown in Fig. 5b, which demonstrates a nonlinear absorption modulation depth (α_s) of 3%, primarily dominated by graphene. Driven by the passive mode-locking mechanism, a pulsed laser with a repetition rate of 14 MHz (Fig. 5c) and an output spectrum width of ~16 nm (Supplementary Fig. 13) was realized, yielding an average FW output power of ~0.5 mW while maintaining stable mode locking. The pulse width could be compressed from ~0.7 ps to ~112 fs through group-velocity-dispersion compensation (Fig. 5d and Supplementary Fig. 14). In addition to the FW light generated by the erbium-doped fibre at 1,560 nm, a frequency-doubling laser at 780 nm was also produced (~10 pW), with the intensity parabolically increasing with the pump source power (Fig. 5e). Note that the integration of mode locking and second-order nonlinear parametric processes within a single fibre ring cavity for frequency-tunable emission was challenging in an all-fibre system previously.

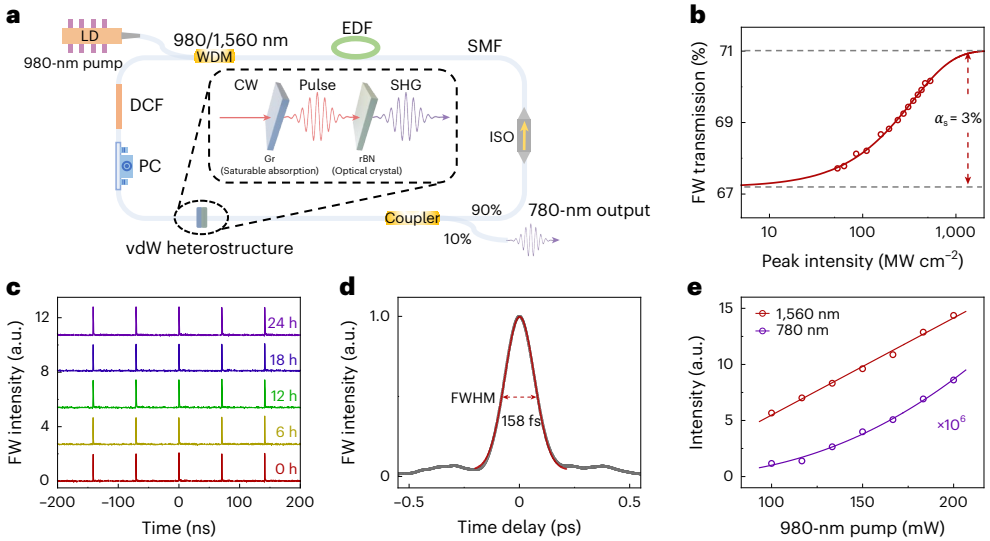


Fig. 5 | All-fibre frequency-doubling pulsed laser with integration of graphene/rBN heterostructure. a, Schematic of the all-fibre intracavity frequency-doubling pulsed laser. In the fibre laser, graphene serves as a nonlinear saturable absorber for mode locking and rBN serves as a nonlinear optical crystal for SHG. The optical components consist of a laser diode (LD), wavelength-division multiplexer (WDM), single-mode fibre (SMF), dispersion compensation fibre (DCF), erbium-doped fibre (EDF), isolator (ISO) and polarization controller (PC). **b**, FW transmission measurement of the graphene/rBN heterostructure integrated optical fibre. The solid curve is fitted according to the experimental data (circles). The nonlinear absorption modulation depth (α_s) is determined to be 3%. **c**, FW output of the long-term pulse train from the all-fibre laser. The repetition rate is determined to be ~14 MHz. **d**, Autocorrelation trace of FW pulse with a full-width at half-maximum of ~158 fs fitted by a Gaussian function, corresponding to a pulse duration of ~112 fs. **e**, Excitation power dependence of FW and SHG intensities in the all-fibre laser. With the increase of the power of the pump laser (at 980 nm), the FW (at 1,560 nm) and SHG (at 780 nm) intensities increase linearly and parabolically, respectively.

Conclusions

In summary, we proposed a phase-matching design on the platform of the fibre end facet and realized an SHG efficiency of 4.1% and photon pair generation via SPDC for vdW crystals in a fibre system. This integration platform exhibits extremely high stability in harsh acceleration, temperature and humidity environments for a long time and over a broad working bandwidth. By constructing nonlinear optical crystals of graphene–rBN heterostructures within a single fibre ring cavity for simultaneous saturable absorption and SHG, we developed an all-fibre frequency-doubling pulsed laser based on a vdW heterostructure. Driven by our phase-matching methodology for vdW crystals on optical fibres, the design and realization of high-efficiency nonlinear and quantum all-fibre systems, such as all-fibre parametric oscillators and all-fibre integrated quantum communication networks, are expected in the near future.

Online content

Any methods, additional references, Nature Portfolio reporting summaries, source data, extended data, supplementary information, acknowledgements, peer review information; details of author contributions and competing interests; and statements of data and code availability are available at https://doi.org/10.1038/s41563-025-02461-x.

References

1. Koester, C. J. & Snitzer, E. Amplification in a fiber laser. *Appl. Opt.* **3**, 1182–1186 (1964).
2. Agrawal, G. P. in *Nonlinear Science at the Dawn of the 21st Century* (eds Christiansen, P. L. et al.) 195–211 (Springer, 2000).
3. Russell, P. Photonic crystal fibers. *Science* **299**, 358–362 (2003).
4. Li, X., Voss, P. L., Sharping, J. E. & Kumar, P. Optical-fiber source of polarization-entangled photons in the 1550 nm telecom band. *Phys. Rev. Lett.* **94**, 053601 (2005).
5. Wang, F. et al. Wideband-tuneable, nanotube mode-locked, fibre laser. *Nat. Nanotechnol.* **3**, 738–742 (2008).
6. Bao, Q. et al. Atomic-layer graphene as a saturable absorber for ultrafast pulsed lasers. *Adv. Funct. Mater.* **19**, 3077–3083 (2009).
7. Sun, Z. et al. Graphene mode-locked ultrafast laser. *ACS Nano* **4**, 803–810 (2010).
8. Martinez, A. & Sun, Z. Nanotube and graphene saturable absorbers for fibre lasers. *Nat. Photonics* **7**, 842–845 (2013).
9. Myers, R. A., Mukherjee, N. & Brueck, S. R. J. Large second-order nonlinearity in poled fused silica. *Opt. Lett.* **16**, 1732–1734 (1991).
10. Kazansky, P. G., Dong, L. & Russell, P. S. High second-order nonlinearities in poled silicate fibers. *Opt. Lett.* **19**, 701–703 (1994).
11. Canagasabey, A. et al. Aperiodically poled silica fibers for bandwidth control of quasi-phase-matched second-harmonic generation. *Opt. Lett.* **35**, 724 (2010).
12. Zhu, E. Y. et al. Direct generation of polarization-entangled photon pairs in a poled fiber. *Phys. Rev. Lett.* **108**, 213902 (2012).
13. Abouraddy, A. F. et al. Towards multimaterial multifunctional fibres that see, hear, sense and communicate. *Nat. Mater.* **6**, 336–347 (2007).
14. St. J. Russell, P., Hölzer, P., Chang, W., Abdolvand, A. & Travers, J. C. Hollow-core photonic crystal fibres for gas-based nonlinear optics. *Nat. Photonics* **8**, 278–286 (2014).
15. Chen, K. et al. Graphene photonic crystal fibre with strong and tunable light–matter interaction. *Nat. Photonics* **13**, 754–759 (2019).
16. Chen, J. et al. Tunable and enhanced light emission in hybrid WS_2-optical-fiber-nanowire structures. *Light Sci. Appl.* **8**, 8 (2019).
17. Zuo, Y. et al. Optical fibres with embedded two-dimensional materials for ultrahigh nonlinearity. *Nat. Nanotechnol.* **15**, 987–991 (2020).
18. Ngo, G. Q. et al. Scalable functionalization of optical fibers using atomically thin semiconductors. *Adv. Mater.* **32**, 2003826 (2020).
19. Jiang, B. et al. High-efficiency second-order nonlinear processes in an optical microfibre assisted by few-layer GaSe. *Light Sci. Appl.* **9**, 63 (2020).

20. Ngo, G. Q. et al. In-fibre second-harmonic generation with embedded two-dimensional materials. *Nat. Photonics* **16**, 769–776 (2022).
21. Li, Y. et al. Nonlinear co-generation of graphene plasmons for optoelectronic logic operations. *Nat. Commun.* **13**, 3138 (2022).
22. Chen, J., Xiong, Y., Xu, F. & Lu, Y. Silica optical fiber integrated with two-dimensional materials: towards opto-electro-mechanical technology. *Light Sci. Appl.* **10**, 78 (2021).
23. Xiong, Y. et al. Twisted black phosphorus-based van der Waals stacks for fiber-integrated polarimeters. *Sci. Adv.* **8**, eabo0375 (2022).
24. Zhang, L. et al. Plasmonic metafibers electro-optic modulators. *Light Sci. Appl.* **12**, 198 (2023).
25. Li, C. et al. Metafiber transforming arbitrarily structured light. *Nat. Commun.* **14**, 7222 (2023).
26. Sun, Z., Martinez, A. & Wang, F. Optical modulators with 2D layered materials. *Nat. Photonics* **10**, 227–238 (2016).
27. Zhao, M. et al. Atomically phase-matched second-harmonic generation in a 2D crystal. *Light Sci. Appl.* **5**, e16131 (2016).
28. Autere, A. et al. Nonlinear optics with 2D layered materials. *Adv. Mater.* **30**, 1705963 (2018).
29. Yu, J. et al. Giant nonlinear optical activity in two-dimensional palladium diselenide. *Nat. Commun.* **12**, 1083 (2021).
30. Abdelwahab, I. et al. Giant second-harmonic generation in ferroelectric $NbOI_2$. *Nat. Photonics* **16**, 644–650 (2022).
31. Xu, X. et al. Towards compact phase-matched and waveguided nonlinear optics in atomically layered semiconductors. *Nat. Photonics* **16**, 698–706 (2022).
32. Guo, Q. et al. Ultrathin quantum light source with van der Waals $NbOCl_2$ crystal. *Nature* **613**, 53–59 (2023).
33. Qi, J. et al. Stacking-controlled growth of rBN crystalline films with high nonlinear optical conversion efficiency up to 1%. *Adv. Mater.* **36**, 2303122 (2024).
34. Ma, C. et al. Strong chiroptical nonlinearity in coherently stacked boron nitride nanotubes. *Nat. Nanotechnol.* **19**, 1299–1305 (2024).
35. Armstrong, J. A., Bloembergen, N., Ducuing, J. & Pershan, P. S. Interactions between light waves in a nonlinear dielectric. *Phys. Rev.* **127**, 1918–1939 (1962).
36. Maker, P. D., Terhune, R. W., Nisenoff, M. & Savage, C. M. Effects of dispersion and focusing on the production of optical harmonics. *Phys. Rev. Lett.* **8**, 21–22 (1962).
37. Shen, Y. R. *Principles of Nonlinear Optics* (Wiley-Interscience, 1984).
38. Lin, J. et al. Broadband quasi-phase-matched harmonic generation in an on-chip monocrystalline lithium niobate microdisk resonator. *Phys. Rev. Lett.* **122**, 173903 (2019).
39. Chen, B.-Q., Zhang, C., Hu, C.-Y., Liu, R.-J. & Li, Z.-Y. High-efficiency broadband high-harmonic generation from a single quasi-phase-matching nonlinear crystal. *Phys. Rev. Lett.* **115**, 083902 (2015).
40. Zhu, S., Zhu, Y. & Ming, N. Quasi-phase-matched third-harmonic generation in a quasi-periodic optical superlattice. *Science* **278**, 843–846 (1997).
41. Hong, H. et al. Twist phase matching in two-dimensional materials. *Phys. Rev. Lett.* **131**, 233801 (2023).
42. Feng, J. et al. Polarization-entangled photon-pair source with van der Waals 3R-WS_2 crystal. *eLight* **4**, 16 (2024).
43. Garay-Palmett, K. et al. Fiber-based photon-pair generation: tutorial. *J. Opt. Soc. Am. B* **40**, 469 (2023).
44. Kallioniemi, L. et al. Van der Waals engineering for quantum-entangled photon generation. *Nat. Photonics* **19**, 142–148 (2024).

Publisher's note Springer Nature remains neutral with regard to jurisdictional claims in published maps and institutional affiliations.

Springer Nature or its licensor (e.g. a society or other partner) holds exclusive rights to this article under a publishing agreement with the author(s) or other rightsholder(s); author self-archiving of the accepted manuscript version of this article is solely governed by the terms of such publishing agreement and applicable law.

© The Author(s), under exclusive licence to Springer Nature Limited 2026

Methods

In situ transfer of twist-rBN on optical fibre end facet

The fabrication is based on a homemade in situ twist fibre transfer system (Supplementary Fig. 3). Polarization-maintaining fibre (Corning PANDA PM980 at 1,064 nm and PM1550 at 1,560 nm) was used. Selected rBN was transferred through a standard process using polypropylene carbonate (PPC). A pulsed laser was transported through the optical fibre (1,064 nm with NPI, Rainbow 1064 OEM and 1,550 nm with NPI, Rainbow 1550 OEM) for the SHG pump. Simultaneously, FW and SHG signals were monitored using a spectrometer (Princeton Instruments, Acton SP-2300).

Numerical calculation of twist phase matching

We used Python code to numerically calculate the result of SHG output intensity with different layer thicknesses and rotation angles in Fig. 2c,e. For the global optimal solution calculation in Fig. 2h, an open source particle swarm optimization (PSO) algorithm was employed to identify the twist-angle sequence that yields the maximum SHG output.

SHG measurements

A mode-locked Ti:sapphire oscillator (Coherent Mira-HP, ~130 fs, 76 MHz) equipped with an optical parametric oscillator (Coherent Mira-OPO-X) was used as the excitation laser for SHG measurement. The excitation light (1,064 nm) is coupled into an optical fibre (Coherent/Nufern, PM980-XP) through an objective (Nikon, ×20, numerical aperture (NA) = 0.30). To accurately obtain the SHG conversion efficiency, we calibrated the coupling efficiency η_{coupling} at first. Then, we measured the FW power P_{ω} in front of the objective lens and the SHG power $P_{2\omega}$ at the optical fibre output, and finally obtained the conversion efficiency $\eta_{\text{SHG}} = \frac{P_{2\omega}}{\eta_{\text{coupling}} \times P_{\omega}}$.

SPDC experiments

A mode-locked 405-nm laser (Coherent chameleon, ~140 fs, 80 MHz) was used as the excitation laser for SPDC measurement. The excitation light is coupled into an optical fibre (Thorlabs, S405-XP) through an objective (Nikon, ×20, NA = 0.30), and interacts with the twist-rBN to generate photon pairs through SPDC. The subsequent light is collimated by another objective (Nikon, ×20, NA = 0.30) and then passes through an interference filter centred at 810 ± 3 nm to remove excitation light. After coupling into the collection fibre, it is split into two beams with a ratio of 50:50 by a fibre beam splitter and detected by two SPDs (EXCELITAS, SPCM-AQRH-16-FC). The detector signals are then transmitted into a time tagger (SIMINICS, MT16) for coincidence detection.

Preparation of encapsulated optical fibre

A single-mode optical fibre (Corning, SMF-28e+) was placed into a quartz tube with an inner diameter slightly larger than that of the optical fibre to increase mechanical stability post-bonding. The end facet of the optical fibre was protruded out of the quartz tube by about 5 mm. Another bare optical fibre was carefully aligned with the rBN fibre by the homemade alignment system including an optical microscope, multi-axis stages and a power meter monitoring transmittance (Supplementary Fig. 9). Covered by refractive index-matched UV curing resin, the fibre junction was thoroughly cured by a UV lamp. The junction was then placed back into the quartz tube, both ends of which were also covered and cured by UV curing resin for reinforcement.

Characterization of the stability

(1) Acceleration: the joint optical fibre is fixed to the end of a reciprocating motor. When the motor is running, the optical fibre can be treated as harmonic oscillation. The reciprocating speed of the motor can be converted into the maximum acceleration applied to the optical fibre. (2) Temperature: The joint fibre is fixed on a heating plate or cooling plate with a temperature controller. (3) Humidity: the optical fibre is placed inside a chamber with a humidifier to control humidity.

Implementation and characterization of the all-fibre frequency-doubling pulsed laser

A pump laser (300 mW, 976 nm) was coupled into the optical fibre ring cavity via a wavelength-division multiplexer (980 nm/1,560 nm) pumping gain medium (60-cm-long erbium-doped fibre, LIEKKI, Er110 4-125). A polarization-independent isolator guaranteed that the laser in the fibre ring propagated along a single direction. Dispersion-compensating fibre was used to compress the pulse width. The pulsed laser (both FW and SHG) was output via a 10% port of a fibre coupler, while the mode-locking condition was optimized by a polarization controller. The output spectra and autocorrelation trace were measured by a spectrometer and an autocorrelator (APE, PulseCheck USB-15). The pulse train was monitored via a photodetector (Thorlabs, DET08CFC/M) and oscilloscope (Tektronix, MDO3104).

Data availability

Relevant data supporting the key findings of this study are available within the article and Supplementary Information. All raw data generated during the current study are available from the corresponding authors upon request.

Code availability

All the codes used in this article for theoretical calculations of twist phase matching can be downloaded at https://github.com/kflin22/twist-optical-crystal.

Acknowledgements

This work was supported by the National Natural Science Foundation of China (12427806 (K. Liu), 52025023 (K. Liu), T2188101 (K. Liu), 12422406 (H.H.), 51991342 (K. Liu), 12374167 (H.H.) and 52172035 (M.W.)), National Key R&D Program of China (2022YFA1403504 (K. Liu), 2021YFA1400201 (H.H.) and 2021YFA1400502 (M.W.)), Guangdong Major Project of Basic and Applied Basic Research (2021B0301030002 (K. Liu)), the Strategic Priority Research Program of Chinese Academy of Sciences (XDB33000000 (K. Liu)), the Research Council of Finland Flagship Programme (320167, PREIN (Z.S.)), ERC (834742 (Z.S.)) and the New Cornerstone Science Foundation through the XPLORER PRIZE (K. Liu).

Author contributions

K. Liu, H.H. and Z.S. conceived the experiments. K. Lin and G.Y. designed and built the in situ twist fibre transfer system. K. Lin and G.Y. performed the optical experiments. K. Lin, Y.Y., D.Y. and Y.W. contributed the theoretical calculations and simulations. K. Lin and J.S. produced the joint fibre and fibre laser. J.Q. and M.W. prepared rBN samples. K. Lin, L.K. and X.Z. contributed coincidence experiments. Z.S. and E.W. suggested the optical experiments. All the authors discussed and contributed to writing the paper.

Competing interests

The authors declare no competing interests.

Additional information

Supplementary information The online version contains supplementary material available at https://doi.org/10.1038/s41563-025-02461-x.

Correspondence and requests for materials should be addressed to Zhipei Sun, Hao Hong or Kaihui Liu.

Peer review information *Nature Materials* thanks Fatih Ilday, Gia Quyet Ngo and the other, anonymous, reviewer(s) for their contribution to the peer review of this work.

Reprints and permissions information is available at www.nature.com/reprints.